JOURNAL OF AIRCRAFT
Vol. 36, No. 5, September–October 1999

Computational Investigation of Simulated Large-Droplet Ice Shapes on Airfoil Aerodynamics

Timothy A. Dunn,* Eric Loth,† and Michael B. Bragg‡
University of Illinois at Urbana–Champaign, Urbana, Illinois 61801

The objective of this research was to study numerically the effects of simulated spanwise-step-ice accretions (resulting from supercooled large-droplet icing conditions) on subsonic aircraft aerodynamics. The investigation was performed with a high-resolution full Navier–Stokes code with a solution-adaptive unstructured grid for both non-iced and iced configurations. The airfoil investigated was a modified NACA 23012 with a simple flap. Simulated ice shapes were tested on the airfoil to determine the sensitivity of ice shape size on airfoil performance and control. Predictions of sectional aerodynamic characteristics for quarter-round ice shape heights of 0.0083 and 0.0139 chords are presented and compared with experimental data. Significant reductions in lift were noted for these relatively small protuberances, which were consistent with experimental findings. The results also indicate good predictive performance for drag, pitching-moment, and hinge-moment variations.

Introduction

THE crash of an ATR-72 commuter aircraft near Roselawn, Indiana, on October 31, 1994, has led to much reevaluation of our current understanding of aircraft icing. The accident is thought to have occurred because of the presence of freezing drizzle, which consisted of droplet sizes much larger than those in the FAR Part 25, Appendix C icing envelopes. Dow provided an excellent overview of the accident and its causes in his 1995 article.[1]

Ice accretions caused by supercooled large droplets (SLDs) can occur on the upper surface behind the active portion of the deicing system boot and can lead to a spanwise-step type of ice accretion protuberance.[2] This can result in changes in the lateral control and the associated hinge moments of the aircraft by altering the flow over the ailerons. It is this degradation in aileron control that is thought to have led to the Roselawn accident. However, the problem is more general since this type of ice accretion can also occur in supercooled droplet clouds of Appendix C size droplets when the air temperature is near freezing. In this case, the accretion occurs behind the boot because of surface water runback and not because of impingement in this region. Also, spanwise-step-ice accretion is not limited to the wing and aileron, but could also occur on the horizontal and the vertical tails and affect other control surfaces including the elevator and rudder, respectively.

In 1996 Bragg[3,4] reviewed the aerodynamic effects of large-droplet ice accretion on aircraft aerodynamics and lateral control based in part on horizontal tail stall data. The spanwise-step-ice accretion, thought to be typical of SLD ice, was shown not only to degrade lift and drag, but also to affect adversely the aileron hinge moment. This hinge-moment effect was traced to the change in the airfoil pressure distribution caused by the separation induced by the ice accretion. Recently, detailed experimental aerodynamic data were obtained for spanwise-step-ice accretions by Lee et al.[5] This study examined lift, drag, pitching moment, and hinge moment for SLD ice shapes and found profound changes compared with those of a clean airfoil.

Similar to experimental studies, previous computational studies of aircraft icing have primarily concentrated on the more common leading-edge ice shapes. Potapczuk[6] used a structured mesh flow (ARC2D) code with an algebraic turbulence model to study a leading-edge glaze-iced NACA 0012 airfoil. Potapczuk compared with experimental results and found reasonable prediction fidelity for lift, drag, and moment curves. The detailed flowfield was also well reproduced. Recently, Caruso and Farshchi[7] used an unstructured mesh flow code and demonstrated high resolution of the detailed flowfield around a leading-edge iced airfoil. Although several calculations were performed, the study focused primarily on the grid-generation procedure and no comparisons with experiment were given.

A limited amount of computational modeling of upper-surface spanwise-step-ice accretions has been conducted. In one of the few relevant studies, Wright and Potapczuk[8] used the ARC2D code to predict the flow over airfoils with simulated SLD shapes from tunnel measurements, LEWICE computational results, and the generic quarter-round shape. The ice accretion caused a large separation bubble that resulted in either a large leading-edge separation or an early trailing-edge separation. The flow was often unsteady at high angles of attack. Recently, Dompierre et al.[9] reported results of computations about an iced NACA 0012 airfoil by using adaptive finite-element methods. One of the ice shapes considered was a quarter-round shape similar to a SLD ice accretion. Although flowfields and a lift curve were plotted, no experimental data were available for comparison.

None of these studies of airfoils with upper-surface spanwise-step-ice accretions examined the aerodynamic distributions and moments as are considered herein. In particular, this paper presents a computational study of the aerodynamic effects of forward-facing quarter-round simulated ice shapes (with heights of approximately 1% of the chord length) on airfoil lift, drag, pitching moment, and hinge moment.

Computational Methodology

Using unstructured adaptive grids is one option to handle efficiently the complex geometries and separation regions associated with multielement iced airfoils. Such grids are typically made up of triangular elements, which can readily conform to surface variations and adapt to local flow gradients. The NSU2D code[10] was designed for treating multielement high-lift airfoils with complex shapes. The code has been successfully applied to a non-iced three-element airfoil by Valarezo and Mavriplis,[11] in which experimental surface pressure and lift at high angle of attack were well reproduced. The NSU2D code was chosen for the present study to compute steady-state solutions.

The NSU2D code uses a Galerkin-based finite-element discretization of the fully compressible Reynolds-averaged Navier–Stokes equations (without a thin-layer assumption). Second- and

---

Received 26 October 1998; revision received 27 March 1999; accepted for publication 3 April 1999.

*Graduate Research Assistant, Department of Aeronautical and Astronautical Engineering. Member AIAA.

†Associate Professor, Department of Aeronautical and Astronautical Engineering. Senior Member AIAA.

‡Professor, Department of Aeronautical and Astronautical Engineering. Associate Fellow AIAA.

fourth-order artificial dissipation are applied to ensure numerical stability. The steady-state convergence was accelerated by use of local time stepping, residual smoothing, and an algebraic multigrid algorithm (AMG). In addition, the unstructured grid methodology of the NSU2D code can easily adapt to multi-element airfoils, complex ice shapes, and regions of high flowfield gradients. It can thus provide high resolution in regions of separated flow, which is necessary to make predictions for the spanwise-step-ice accretions considered herein.

The code supports both laminar and turbulent flow. The turbulent flow was modeled with the Spalart–Allmaras model,[12] which has been shown to reproduce free-shear-layer and boundary-layer behavior accurately. The transition point must be user specified and was herein predicted a priori by use of the integral boundary-layer program of XFOIL.[13] This program incorporates an e^n-type amplification formulation for determining the transition location. To account for variations in the predicted lift of XFOIL, a lift-corrected angle of attack was used when the transition point was being computed. For the cases with a boundary-layer trip placed on the airfoil, the transition was assumed to occur at whichever came first: the trip location or the transition location predicted by XFOIL.

Validation with Non-Iced Airfoils

To determine grid sensitivity/optimization and prediction robustness, the code was validated with some canonical experimental sets for a non-iced NACA 0012 airfoil. For these simulations, the computational domain was a square region, 40 × 40 chords, with the airfoil in the center. Far-field boundary conditions were used on the outer boundary. The high-resolution grid contained approximately 50,000 nodes and 600 points on the airfoil surface. In the direction normal to the airfoil surface, there were approximately 50 nodes within the boundary layer with the first node approximately at a y/c of 2×10^{-6} and a 15% successive increase in grid size away from the wall (where c is the airfoil chord length).

The predictions obtained from the NSU2D code are first compared with the experimental data of Harris.[14] This data set was chosen because of its accepted reliability[15] and because of the abundance of other computational fluid dynamics (CFD) validations that have used the data.[16] The data were collected for a Mach number of 0.3 and a Reynolds number of 3×10^6 with transition trips placed at the 5% chord location on the upper and the lower surfaces. The experimental data were corrected by use of the linear method for simulating wall interference provided by Harris.

Figure 1 shows the normal force coefficient C_n as a function of angle of attack α, drag coefficient C_d, and moment coefficient about the quarter chord C_m. The computational results are reported for only those angles that demonstrated convergence. Typically, the maximum converged angles correlated with the maximum lift conditions. The computational results for normal force were in good agreement with the experimental Harris data for each angle of attack up to the maximum lift point. The results for normal force vs drag coefficient also compared reasonably well. The results at the lower angles of attack matched the experimental data within a few percent. The code somewhat underpredicted the drag at the higher angles of attack, potentially because of the difficulties associated with selecting a transition location once transition moved forward of the transition trip. The code also predicted the moment coefficient for the range of angles.

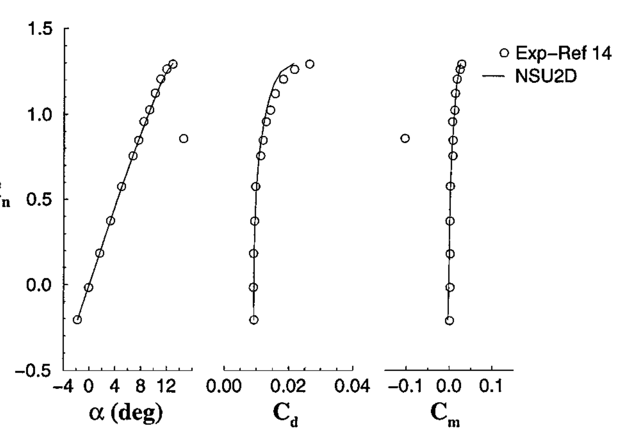

Fig. 1 Aerodynamic coefficients for a NACA 0012 airfoil.

The pressure coefficient distribution along the airfoil surface is plotted in Fig. 2 for an angle of attack of 11.90 deg. The code accurately reproduced the airfoil surface-pressure fields, including the pressure spike at the airfoil's leading edge. Detailed grid resolution studies were conducted to note effects of various grid-generation parameters and determine values required for accurate resolution. Studies in which the number of nodes was increased by fourfold yielded less than 2% change in the lift, drag, or any part of the pressure distribution. Therefore the solution is considered reasonably grid independent.

The second set of validation calculations on the NACA 0012 were intended to assess the ability of the code to predict chord Reynolds number Re and freestream Mach number M effects by comparing them with the data of Ladson.[17] The results for fixed Mach numbers of 0.15 and 0.30 for Reynolds numbers of 2×10^6, 4×10^6, and 6×10^6 are given in Fig. 3. For both Mach numbers, the code was able to predict the slight increases in both the lift curve slope and the maximum lift for increases in Reynolds number. However, in all cases there was a slight overprediction of the lift, especially at the lower Mach number. Comparison of the two figures reveals that the computations successfully predicted both the slight increase in slope and the significant decrease in maximum lift for an increase in Mach number. Therefore the code was generally able to predict trends that were due to both Mach number and Reynolds number variations for the lift curve slope and for the maximum lift of the non-iced NACA 0012 airfoil.

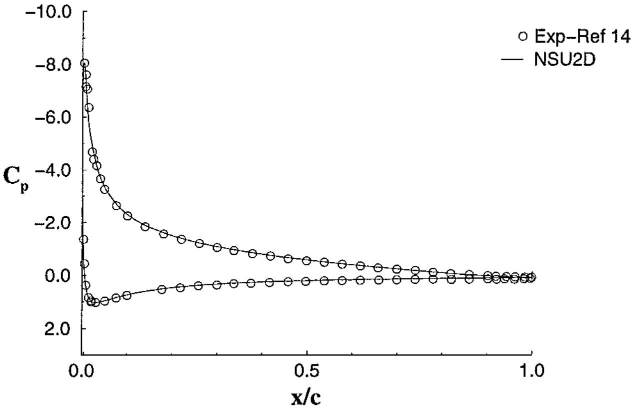

Fig. 2 Surface-pressure distribution for a NACA 0012 airfoil at α = 11.90 deg.

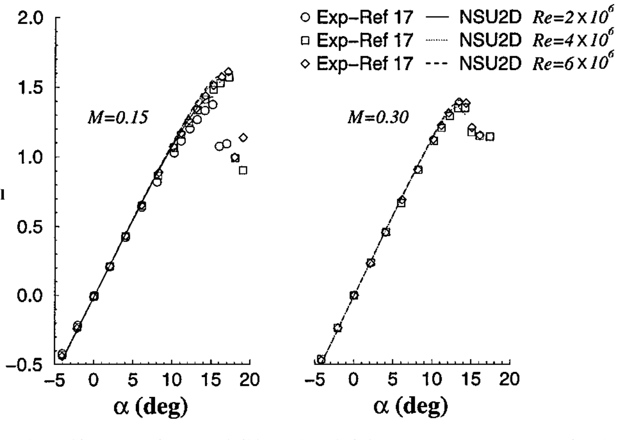

Fig. 3 Lift curve for a NACA 0012 airfoil at Mach numbers of 0.15 and 0.30.

Validations with Backward-Facing Step

The ability to predict separating and reattaching shear flows is critical for accurately predicting iced-airfoil aerodynamics. The backward-facing step is one of the least complex geometries that provides this type of flow. Because of the extensive amount of experimental and computational research that has been conducted on step flows, it is an obvious choice for validation. An important aspect of an iced-airfoil flowfield is the associated adverse pressure gradient throughout the separation region. To simulate this pressure gradient effect while keeping the simple geometry of the backstep, the channel wall opposite to the step can be diverged. The experimental data of Driver and Seegmiller[18] are of this form and were used herein for comparison.

Because the NSU2D code was designed to solve compressible flows around airfoils, conventional methods of setting up the backward-facing step problem are inconvenient. Therefore the backstep was modeled with an enclosed solid surface placed within a divergent channel. The surface was shaped to provide an upper-surface backstep (as well as a lower-surface backstep for flow symmetry) with long upstream and downstream extensions for boundary-layer development and reattachment. The upstream length was determined such that the resulting boundary-layer profile at the top of the step matched the experimental data. The surface of the backstep was modeled with no-slip (Navier–Stokes) boundary conditions, and the opposite wall was modeled with slip (Euler) boundary conditions in order to reduce the number of grid points required in the simulation.

Reattachment length was examined for prediction fidelity because it is a sensitive parameter of the flow behavior. Figure 4 plots the reattachment length vs the top-wall deflection angle δ. Along with the experimental data, the NSU2D predictions are also compared with computations using modified versions of the k–ϵ and algebraic-stress turbulence models (ASM) presented by Driver and Seegmiller. Overall, the NSU2D code appears to have reproduced the experimental reattachment lengths reasonably well, including the trend of increasing with greater pressure gradient. However, the NSU2D code slightly underpredicted the reattachment length as the deflection angle was increased. It should be noted that modification of the Spalart–Allmaras turbulence model to include rotational terms has been found to have a negligible impact on the separated backstep predictions.[19]

Figure 5 plots the variation in pressure coefficient past the backstep for top-wall deflection angles of 0 and 6 deg. Although the simulations showed reasonable fidelity, the predictions for both angles initially underestimated the pressure just after the step, followed by a slightly faster pressure recovery than the experiment. The pressure far downstream of reattachment for both angles was slightly overpredicted by the NSU2D code. This is attributed to the Euler boundary conditions used along the top wall since the presence of the boundary layer on this wall in the experiments effectively reduced the deflection angle and therefore reduced the downstream pressure.

Figure 6 shows the experimental and the computational mean velocity profiles for a variety of streamwise positions. Results for top-wall deflection angles of 0 and 6 deg are shown. The boundary layer ahead of the step was reasonably reproduced, indicating that the computational setup was appropriate for this problem. The general shape of the velocity profiles after the step was also well predicted. As mentioned by Driver and Seegmiller, the velocity profiles compared with the measured reattachment locations indicate that in the downstream portion of separation the flow reversal was confined to a long, thin region that could not be resolved experimentally. This thin region of reverse flow was predicted by the current computations. Far downstream of reattachment, the edge velocity of the computations was less than the edge velocity of the experiment, especially in the 6-deg deflection case. Once again, this was due to the higher numerical downstream pressure caused by the Euler boundary condition on the upper wall. Overall, the NSU2D code was able to predict reasonably the reattachment and the flowfield for the backward-facing step with a mild pressure gradient.

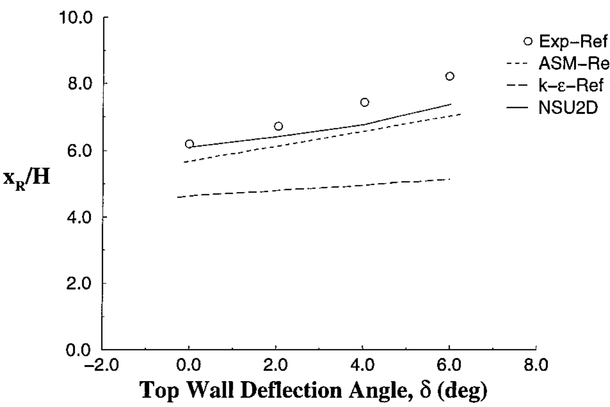

Fig. 4 Reattachment length past a backward-facing step.

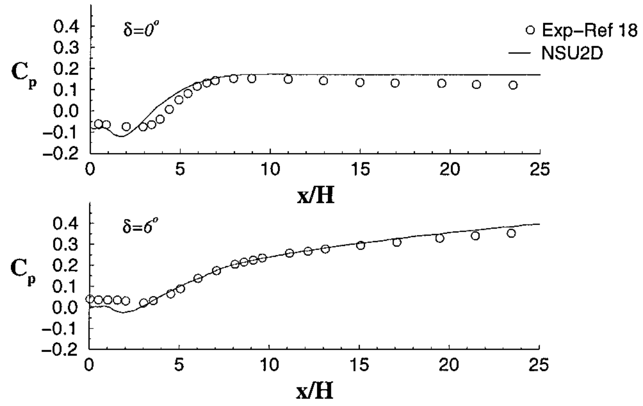

Fig. 5 Pressure distribution past a backward-facing step.

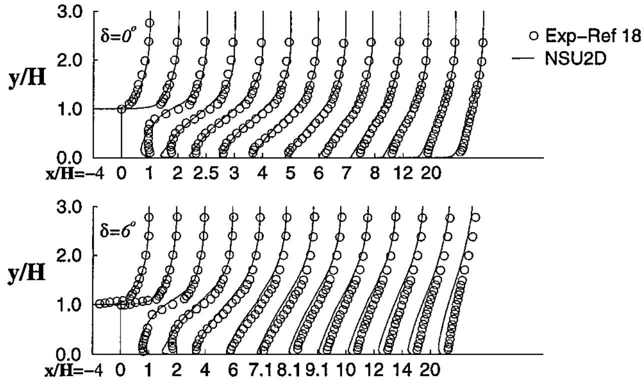

Fig. 6 Mean velocity profiles past a backward-facing step.

Iced-Airfoil Results

In this section, we consider the aerodynamic influence of a quarter-round ice shape computationally by varying its maximum height. In addition, a case with no ice shape that includes only the boundary-layer trip is used as a reference condition. The experimental data of Lee et al.[5] are used for comparison. The data were taken for $M = 0.2$ and $Re = 1.8 \times 10^6$ by use of a modified NACA 23012 airfoil. The modified airfoil geometry is described in the experimental data set of Lee et al.[5] As above, the code was run for all experimental angles but only conditions that were fully converged are reported in the figures.

Numerical Implementation

The presence of the quarter-round ice shape on the airfoil required additional consideration for the prediction methodology. The protuberance can cause a large separation bubble that initiates at the top of the shape because of its sharp corner. This configuration fortunately eliminates the problem of predicting the separation point of the free-shear layer, which can be difficult to simulate accurately on smooth surfaces. For entrainment along the free-shear layer itself, the flow can be considered as fully developed turbulent in a small fraction of a step height downstream of the separation point for the Reynolds numbers considered herein.[20] Therefore the entire free-shear layer and reattachment regions were modeled as turbulent.

All experimental results considered herein used trip strips placed at 5% chord. Therefore, for all positive angles of attack, the transition point for the iced airfoil was always taken as the trip location. This is because the iced case was limited to low lift coefficients such that the lift-corrected non-iced XFOIL transition was never further upstream than the trip location. Computations for which the trip location was altered did not change the results significantly. However, for negative angles of attack, the transition location on the lower surface moved forward of the transition trip. Therefore the transition position for the lower surface was taken at the leading edge for all negative angles of attack.

The condition of the flow through the flap gap (laminar, turbulent, or transitional) was also difficult to judge because it contained two thin channels surrounding a cavity and could be subjected to a variety of pressure differences and Reynolds numbers. Fortunately, no significant changes were found if the gap was modeled as turbulent or laminar for cases with no flap deflection. Therefore the region was always modeled as fully turbulent. However, it was noted that there was significant sensitivity of the flow solution to the width of the thin channel, where velocities of more than one half of the freestream velocity can be found. This was unfortunate because the experimental setup made accurate measurement of the gap thickness difficult and there may have been some spanwise variation that was due to loading as well. Therefore it is expected that some of the variation between the clean-airfoil predictions and the experimental data was caused by an inaccurate geometry definition around the flap gap. However, this is not expected to have a large effect on the iced-airfoil predictions as the pressure gradient across the flap gap was very small compared with that of the clean airfoil.

It was also desired to use a grid that formally included tunnel-wall effects. Therefore the present iced-airfoil predictions were based on the upper and the lower tunnel walls directly modeled within the computation by assuming slip (Euler) boundary conditions at these surfaces. To validate this approach for the NSU2D code, simulations were conducted with free boundary conditions in the far-field along with simulations in which the tunnel walls were modeled directly. The simulations with tunnel walls were theoretically corrected a posteriori to an infinite domain by use of the theory of Rae and Pope[21] and compared with the predictions by use of far-field boundary conditions. In general, there were insignificant differences (e.g., less than 1%) between these two methods for prediction of the lift and the drag.

Because of the presence of the ice shape and flap, a much finer grid was used for the iced-airfoil calculations than was used in the validation calculations. The initial grids contained approximately 100,000 nodes and 1300 points along the airfoil surface. The grid points were clustered around the ice shape and within the separation region. The spacing of the first grid point normal to the airfoil surface was 1×10^{-6} chord lengths with a 15% successive increase in grid size away from the wall. A portion of the grid surrounding the airfoil geometry is shown in Fig. 7.

Figure 8a shows a closeup of the initial grid generated by the NSU2D code near the ice shape for $\alpha = 0$ deg. Although this grid was highly refined, it was deemed insufficient with respect to the resolution of the resulting free-shear layer. Therefore grid adaptivity was used with a technique similar to that of Mavriplis.[22] However, in the present methodology the grid refinement was based on a flow variable gradient within a particular triangle, whereas Mavriplis based it on the gradient along an edge. The present adaptation technique essentially subdivides any element for which gradients in the chosen parameter exceed a certain tolerance level. In addition, the present computations included a modification to allow interpolation of the original-grid flowfield results onto the adapted-grid domain for further computation. Figure 8b shows the grid resulting from one adaptation based on gradients in absolute velocity. Figure 8c shows the corresponding velocity contours of the initial solution for this angle. Note that additional grid points have been clustered around the separation point and along the high-velocity gradients of the downstream free-shear layer. The adaption increased the number of grid points by approximately 25%. All iced computations presented here used this same adaption strategy. Using additional refinement and adaption was also investigated, but there were no significant differences in flow prediction.

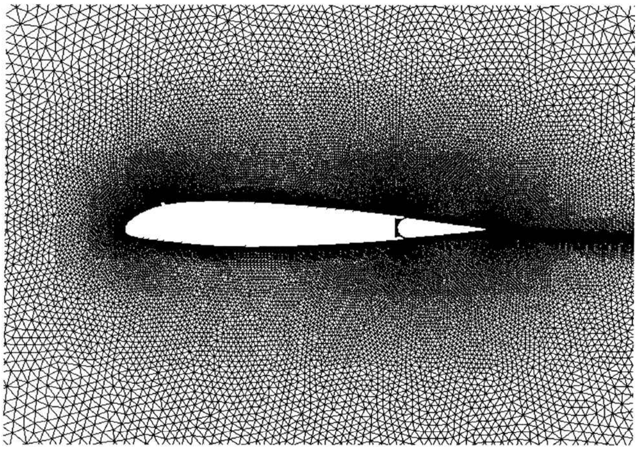

Fig. 7 Grid surrounding the airfoil geometry.

The computations were completed on both the Aeronautical and Astronautical Engineering Department's SGI workstations and the NCSA (National Center for Supercomputing Applications) SGI Power Challenge Array and Origin 2000. Iced-airfoil calculations on the SGI Origin 2000 with three multigrid levels took approximately 20 s of CPU time per cycle for each angle. Iced calculations required approximately 1000 cycles for convergence.

Force and Moment Results

The lift curves of airfoils with $k/c = 0.0$ (non-iced), 0.0083, and 0.0139 quarter-round ice shapes located at $x/c = 0.10$ are shown in Fig. 9. In general, the NSU2D predictions for the non-iced case exhibited good comparison with the experimental results, although the slope of the lift curve and the maximum lift coefficient were overestimated, similar to the predictions of the low Reynolds number cases computational validations of Fig. 3. A portion of this discrepancy can be attributed to the slight difference in flap gap geometry for the experiment and the computations. The significant reduction in lift curve slope and the dramatic reductions in maximum lift coefficient and maximum lift angle caused by the ice shape presence were predicted reasonably well by the NSU2D code. However, the NSU2D predictions exhibited a weaker break in the lift curve slope than that shown by the experiments. Also, no noticeable maximum lift condition was seen in the NSU2D predictions. This can probably be attributed to possible large-scale unsteady separation bubble behavior in the measurements at high angles of attack, which the steady-state calculations cannot predict.

Figure 10 shows the drag predictions. The trends that were due to the presence and the height change of the ice shape were well predicted by the NSU2D code. Considering the large amount of separation occurring for the iced-airfoil flows, the performance of the simulations was quite encouraging. The slight underprediction of the drag coefficient at higher lift conditions of the non-iced case was consistent with the validation computations (Fig. 1).

Figure 11 shows the pitching-moment coefficient distribution with angle of attack. The NSU2D code predicted the strong dropoff in moment at positive angles of attack as the ice shape increased in size. However, the computations did not predict the increase in moment coefficient for angles of 7 deg or more. The non-iced-airfoil case showed large deviations from the experiment of the order of 0.02. Once again, this was due to a combination of small differences

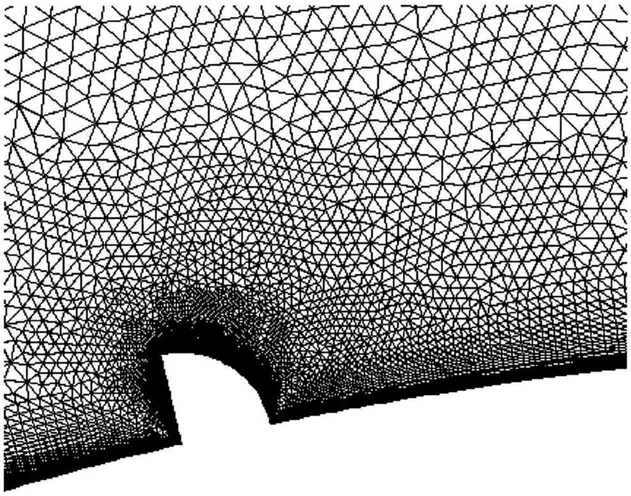

a) Original grid near simulated ice shape

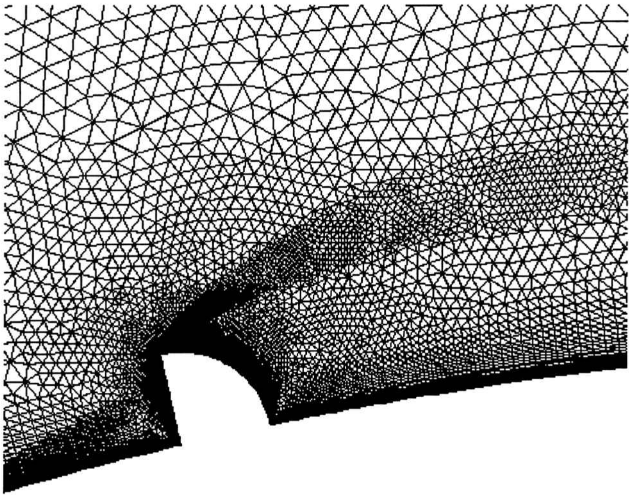

b) Adapted grid near simulated ice shape

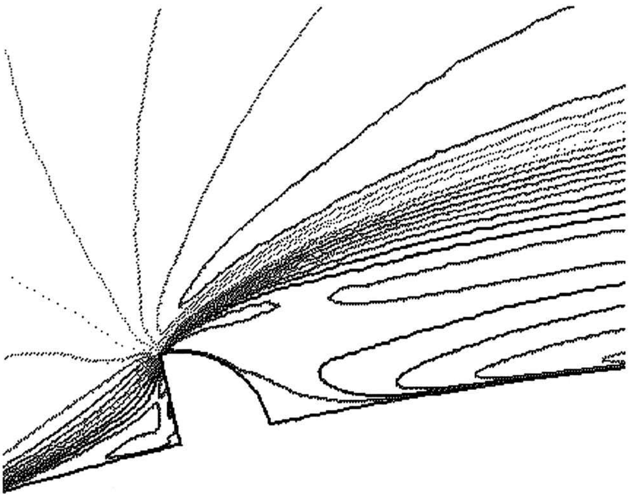

c) Absolute velocity contours for original grid

Fig. 8 Effect of grid adaption near the ice-shape.

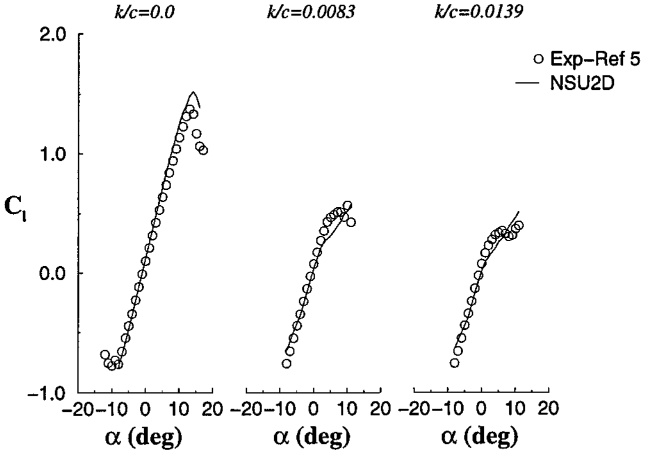

Fig. 9 Effect of ice shape height on lift.

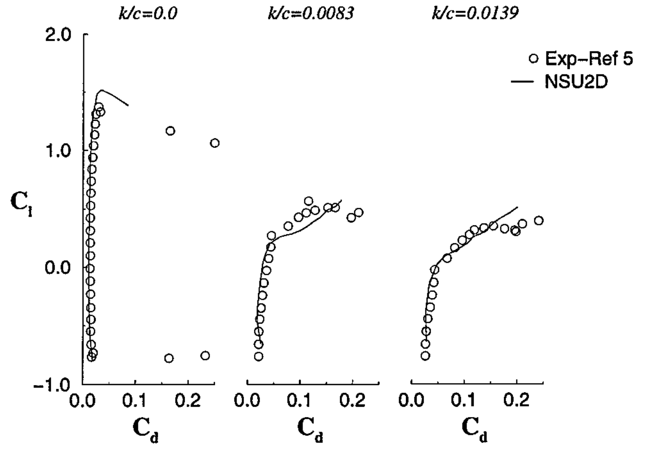

Fig. 10 Effect of ice shape height on drag.

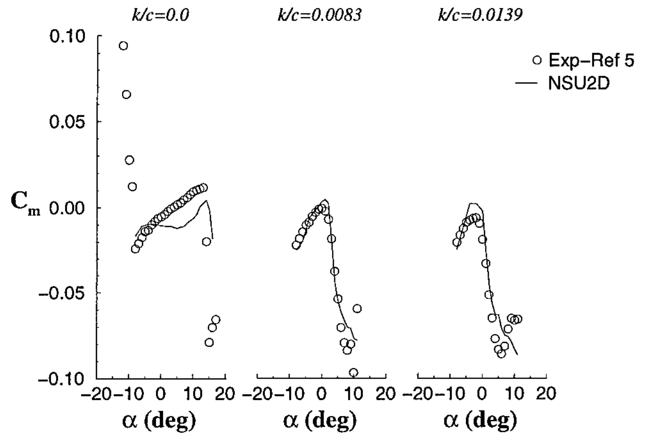

Fig. 11 Effect of ice shape height on pitching moment.

in the pressure distribution both on the forward upper surface of the quarter chord and on the lower surface aft of the quarter chord caused by insufficient mass flow through the flap gap.

Perhaps the most important aerodynamic coefficient with respect to aircraft control is the hinge moment. The comparison between computation and experiment of this sensitive parameter is shown in Fig. 12. Again the NSU2D code successfully predicted the qualitative trends resulting from the presence and change in height of the ice shape. In particular the increased dropoff in C_h at high angles of attack was reproduced.

The above results indicate that the NSU2D code correctly predicted the trends of all the major aerodynamic features associated with the ice shape for these experimental conditions. In addition, the quantitative comparison was reasonable for many of the present conditions.

Flowfield Details

In this subsection we consider some of the aerodynamic details responsible for the integrated quantities discussed above. The pressure distributions for $k/c = 0.0$, 0.0083, and 0.0139 quarter-round

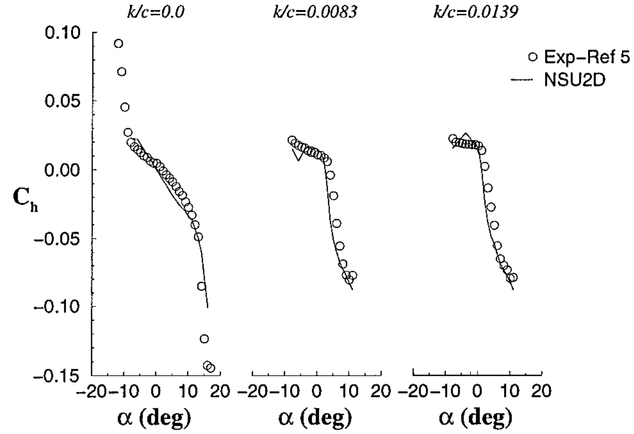

Fig. 12 Effect of ice shape height on hinge moment.

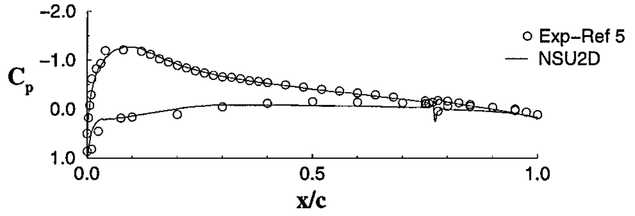

a) *k/c* = 0.0

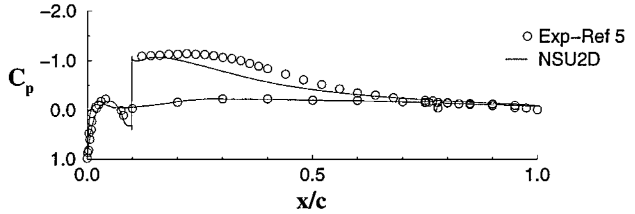

b) *k/c* = 0.0083

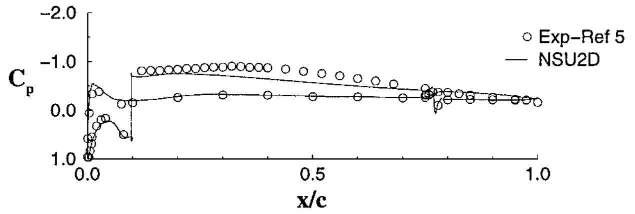

c) *k/c* = 0.0139

Fig. 13 Effect of ice shape height on pressure distribution at α = 3 deg.

ice shape configurations at $\alpha = 3$ deg are plotted in Fig. 13. The noniced pressure distribution (Fig. 13a) shows a small overprediction of the suction pressure on the forward upper surface and an overprediction of the aft lower surface pressure. This was mentioned above with respect to the deficiency of the moment coefficient predictions of Fig. 11. It is expected that the flap gap geometry was largely responsible for this discrepancy. The plots show that the presence of the ice shape (Figs. 13b and 13c) caused an increase in pressure at the leading edge, i.e., the suction peak was reduced. This created a much more rear-loaded airfoil with a subsequent change in the pitching moment and loss in lift. Also, the pressure along the lower surface decreased as the ice shape size was increased, resulting in a further loss in lift. In the following paragraphs additional details of the flowfield along with the fidelity of the computational results are addressed for the $k/c = 0.0083$ ice shape.

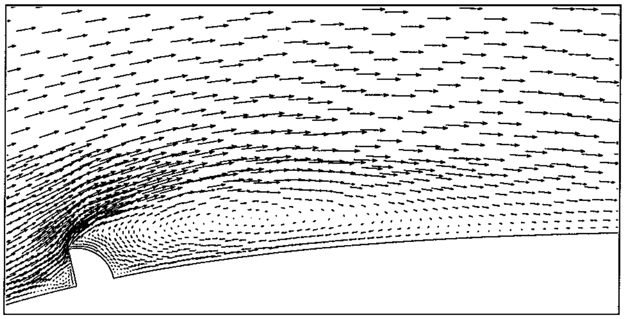

Fig. 14 Velocity vectors at sample locations around a NACA 23012m at α = – 6 deg with *k/c* = 0.0083 ice shape.

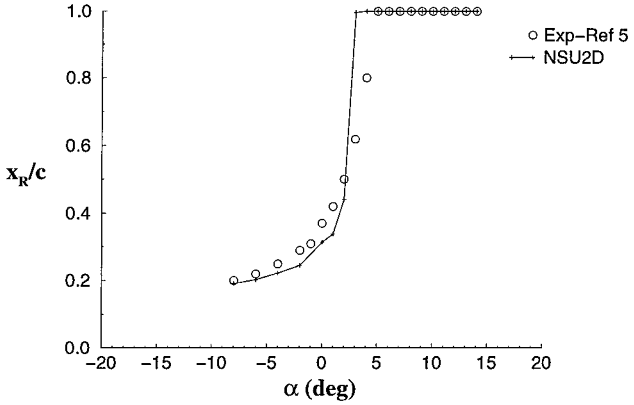

Fig. 15 Reattachment locations of the aft-ice separation bubble for an ice shape with height *k/c* = 0.0083.

Figure 14 plots selected velocity vectors within the separation bubble aft of the $k/c = 0.0083$ ice shape for $\alpha = -6$ deg. Note that, if all the velocity vectors were plotted, the figure would be too dense to be clear (recall the mesh detail given in Fig. 8b). The velocity vectors show the large aft separation bubble extending from the top of the ice shape with an initial expansion upward. At this low angle of attack, the separation region was quite thin and remained fairly close to the airfoil. The small recirculation region upstream of the ice shape showed a vertical extent that was less than the top of the ice shape, a result that is consistent with the buff-body experiments of Winkler.[23]

Figure 15 plots the reattachment length for the separation bubble aft of the ice shape verses the airfoil's angle of attack for the $k/c = 0.0083$ ice shape. Although no experimental flow visualization was performed for this case, reattachment lengths obtained through analysis of the experimental pressure distributions are plotted for comparison. The computational reattachment lengths were determined by use of the predicted skin friction along the airfoil surface. The figure shows that the bubble has almost exponential growth, as the reattachment length grew slowly at the low angles then quickly at the larger angles until the bubble reached the trailing edge. The computations predicted a somewhat shorter reattachment length at the low angles, which is consistent with the backward-facing step results in Fig. 4. Between 2 and 3 deg the computations showed very rapid bubble growth and the predicted separation region reached the trailing edge before the experimental bubble. This is the expected reason for the earlier break in the hinge-moment predictions. The predictive differences found between the experimental and the computational reattachment lengths at the higher angles are attributed to unsteady effects at the high angles and difficulties in predicting the flow through the flap gap.

Figures 16–18 plot the pressure distribution along the airfoil with the $k/c = 0.0083$ ice shape for $\alpha = -6$, 0, and 6 deg, respectively (recall Fig. 13b for $\alpha = 3$ deg). Computationally predicted streamlines are also shown for each angle as a reference for the bubble behavior. For each of these plots, the NSU2D code accurately predicted the pressure over the majority of the airfoil surface. The code gave excellent agreement in the nonseparated regions of the airfoil, i.e., along the lower surface and along the upper surface in front of the ice shape. This is especially noticeable in the $\alpha = -6$ deg case (Fig. 16) in which the pressure spike at the leading edge of the lower

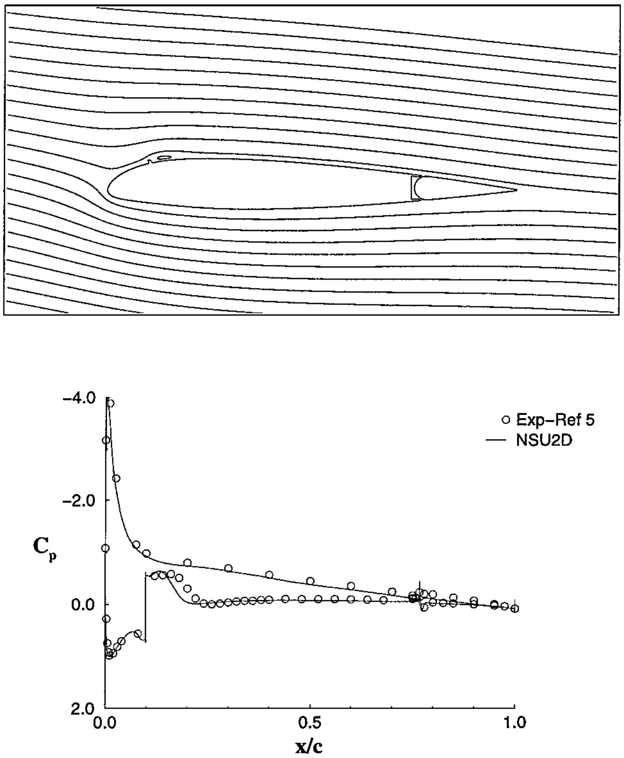

Fig. 16 Streamlines and surface-pressure distributions for a NACA 23012m at $\alpha = -6$ deg with $k/c = 0.0083$ quarter-round ice shape.

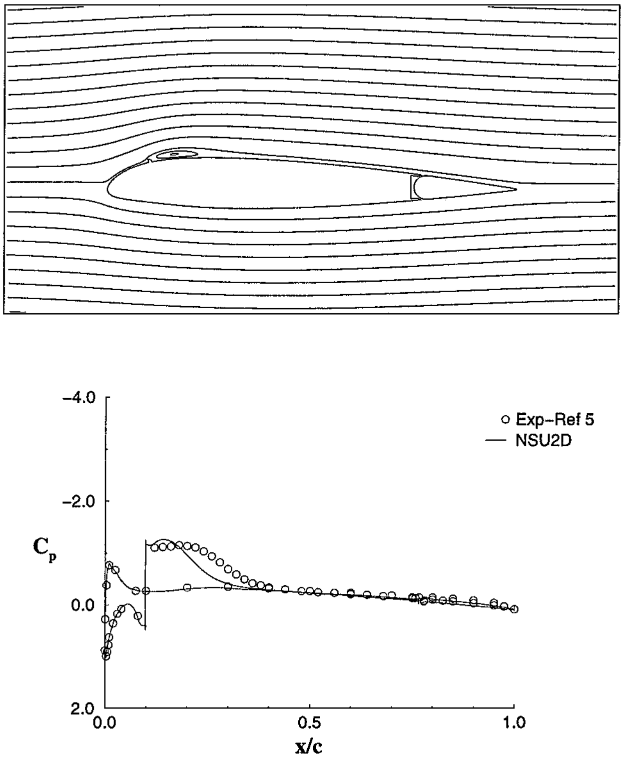

Fig. 17 Streamlines and surface-pressure distributions for a NACA 23012m at $\alpha = 0$ deg with $k/c = 0.0083$ quarter-round ice shape.

surface was well predicted. The code accurately predicted the pressure increase in the stagnation region ahead of the ice shape, as well as the magnitude of the suction peak occurring downstream of the ice shape. However, similar to the results for the backward-facing step (Fig. 5), the NSU2D code displayed a much faster pressure recovery than the experimental data in the large separation region aft of the ice shape. This discrepancy in the separation region became more severe as the angle of attack was increased. This error in pressure recovery is thought to be due to the turbulence model's inadequately predicting the amount of entrainment within the shear layer. This is an area that should be investigated further and may require modification of the current turbulence model.

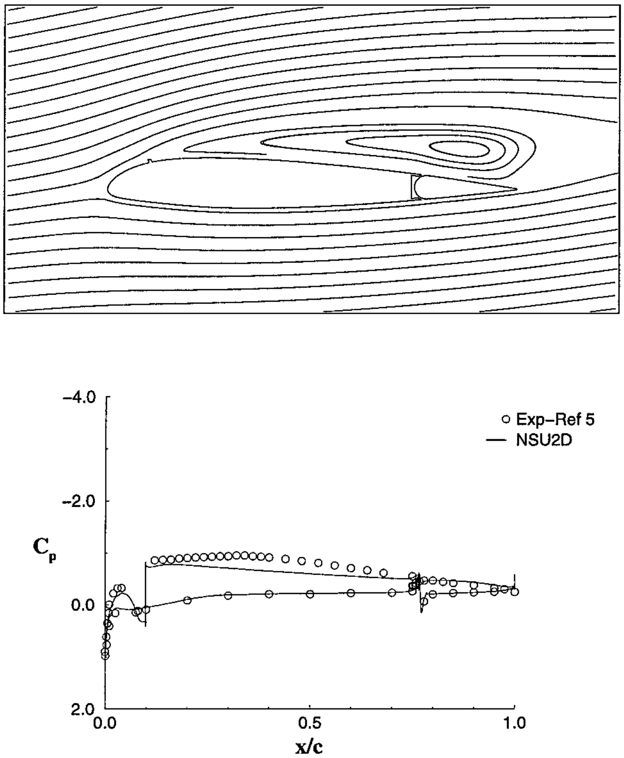

Fig. 18 Streamlines and surface-pressure distributions for a NACA 23012m at $\alpha = 6$ deg with $k/c = 0.0083$ quarter-round ice shape.

Comparisons of the pressure distribution at higher angles (Fig. 18) reveal a similar level of discrepancy despite having a fully separated flow. This is attributed to the fact that the reattachment point had become fixed at the trailing edge for both the experiments and the computations (a reattachment condition more easily predicted). It is remarkable that in all of these cases, the differences in the pressure distribution did not significantly affect the aerodynamic moment coefficients. This was because the pressure discrepancies were centered primarily around the quarter-chord location and therefore tended to cancel themselves out once levered about the hinge line.

Analysis of the aerodynamic coefficients, reattachment lengths, pressure distributions, and flowfield plots indicates three general regimes of flow phenomena that can be isolated: linear, nonlinear, and fully separated. The linear regime is associated with low angles of attack (approximately less than 0 deg in this case). Here the separation bubble remains close to the airfoil surface, and the chordwise growth of the bubble as the angle of attack is increased is fairly slow. At higher angles of attack (at approximately 0–4 deg), the airfoil displays the behavior of the nonlinear regime, yielding a break in the aerodynamic forces and moments. Here the bubble displays rapid growth over a relatively small range of angle of attack (Fig. 15). Unsteady flow behavior is expected to start developing in this regime. Once the separation region reaches the trailing edge the airfoil is in the fully separated regime ($\alpha > 4$ deg). Here the bubble quickly begins to extend away from the airfoil and into the outer flowfield. With this type of bubble, large-scale vortex shedding is more likely to occur. This type of unsteady phenomenon cannot be captured with the current steady-state computational strategy, and therefore the computational results are questionable at these angles. As such, further improvements of the NSU2D prediction accuracy may be realized by use of an unsteady simulation procedure similar to that used by Potapczuk.[6] Modification of the code to allow unsteady flow and examinations of the effect of ice shape location and flap deflection influence are subjects of current research for this ongoing investigation. In addition, future research will consider additional airfoil geometries, Reynolds number dependence, and a more detailed study of the fluid dynamics.

Conclusions

The NSU2D code was successfully validated with several non iced-airfoil experiments, including effects of Reynolds number and Mach number and a backward-facing step. The computational results for the iced-airfoil experiments indicate that the NSU2D code correctly predicted the trends of all the major aerodynamic features associated with the ice shape presence. In particular, the NSU2D code gave predictions of pitching moment and hinge moment that were well correlated with the experimental data for both the non-iced airfoil and the iced airfoil. This is important since prediction of the ice shape effect on hinge moment is critical to forecasting the possible influence of SLDs on aileron or rudder control. The lift and drag predictions were also quite reasonable up to the point at which the flow was fully separated over the airfoil.

Acknowledgments

This work was supported by the Federal Aviation Administration under grant DTFA MB 96-6-023 with James Riley as technical monitor. The computations were performed with support from the National Computational Science Alliance (NCSA) under grant CTS970036N and utilized the NCSA SGI/CRAY Origin2000 and POWER CHALLENGE array. The authors gratefully acknowledge the assistance of Gene Hill, Tom Bond, Mark Potapczuk, Dimitri Mavriplis, Sam Lee, and Holly Gurbacki.

References

[1] Dow, J. P., Sr., "Roll Upset in Severe Icing," Federal Aviation Administration, Aircraft Certification Service, Washington, DC, Sept. 1995.

[2] National Transportation Safety Board, "Icing Tanker Test Factual Report," Docket SA-512, Exhibit 13B, DCA95MA001, Washington, DC, Feb. 1995.

[3] Bragg, M. B., "Aircraft Aerodynamic Effects Due to Large Droplet Ice Accretions," AIAA Paper 96-0932, Jan. 1996.

[4] Bragg, M. B., "Aerodynamics of Supercooled-Large-Droplet Ice Accretion and the Effect on Aircraft Control," *Proceedings of the FAA International Conference on Aircraft Inflight Icing*, Vol. 2, DOT/FAA/AR-96/81,II, Federal Aviation Administration, Washington, DC, 1996, pp. 387–399.

[5] Lee, S., Dunn, T., Gurbacki, H. M., Bragg, M. B., and Loth, E., "An Experimental and Computational Investigation of Spanwise-Step-Ice Shapes on Airfoil Aerodynamics," AIAA Paper 98-0490, Jan. 1998.

[6] Potapczuk, M., "Numerical Analysis of a NACA0012 Airfoil with Leading Edge Ice Accretions," AIAA Paper 87-0101, Jan. 1987.

[7] Caruso, S. C., and Farshchi, M., "Automatic Grid Generation for Iced Airfoil Flowfield Predictions," AIAA Paper 92-0415, Jan. 1992.

[8] Wright, W. B., and Potapczuk, M. G., "Computational Simulation of Large Droplet Icing," *Proceedings of the FAA International Conference on Aircraft Inflight Icing*, Vol. 2, DOT/FAA/AR-96/81,II, Federal Aviation Administration, Washington, DC, 1996, pp. 545–555.

[9] Dompierre, J., Cronin, D. J., Bourgault, Y., Baruzzi, G. S. Habashi W. G., and Wagner, G. A., "Numerical Simulation of Performance Degradation of Ice Contaminated Airfoils," AIAA Paper 97-2235, June 1997.

[10] Mavriplis, D., "Multigrid Solution of Compressible Turbulent Flow on Unstructured Meshes Using a Two-Equation Model," NASA CR-187513, NASA Langley Research Center, ICASE, Jan. 1991.

[11] Valarezo, W. O., and Mavriplis, D., "Navier–Stokes Applications to High-Lift Airfoil Analysis," AIAA Paper 93-3534, Aug. 1993.

[12] Spalart, P. R., and Allmaras, S. R., "A One-Equation Turbulence Model for Aerodynamic Flows," AIAA Paper 92-0439, Jan. 1992.

[13] Drela, M., "XFOIL 6.6 User Primer," MIT Aero & Astro Engineering, Massachusetts Inst. of Technology, Cambridge, MA, March 1996.

[14] Harris, C. D., "Two-Dimensional Aerodynamic Characteristics of the NACA 0012 Airfoil in the Langley 8-Foot Transonic Pressure Tunnel," NASA TM-81927, 1981.

[15] McCroskey, W. J., "A Critical Assessment of Wind Tunnel Results for the NACA 0012 Airfoil," AGARD, Aerodynamics Data Accuracy and Quality: Requirements and Capabilities in Wind Tunnel Testing, July 1988.

[16] Holst, T. L., "Viscous Transonic Airfoil Workshop Compendium of Results," AIAA Paper 87-1460, June 1987.

[17] Ladson, C. L., "Effects of Independent Variation of Mach and Reynolds Numbers on the Low-Speed Aerodynamic Characteristics of the NACA 0012 Airfoil Section," NASA TM-4074, 1988.

[18] Driver, D. M., and Seegmiller, H. L., "Features of a Reattaching Turbulent Shear Layer in Divergent Channel Flow," *AIAA Journal*, Vol. 23, No. 2, 1985, pp. 163–171.

[19] Spalart, P. R., and Shur, M., "On the Sensitization of Turbulence Models to Rotation and Curvature," *Aerospace Science and Technology*, Vol. 1, No. 5, July 1997, pp. 297–302.

[20] Oakley, T., Loth, E., and Adrian, R., "Cinematic Particle Image Velocimetry of a Turbulent Free Shear Layer," *AIAA Journal*, Vol. 34, No. 2, Feb. 1996, pp. 299–308.

[21] Rae, W. H., and Pope, A., *Low-Speed Wind Tunnel Testing*, Wiley, New York, 1984, pp. 349–362.

[22] Mavriplis, D., "Turbulent Flow Calculations Using Unstructured and Adaptive Meshes," NASA CR-182102, NASA Langley Research Center, ICASE, Sept. 1990.

[23] Winkler, J. F., "Local Flowfield About Large Distributed Roughness Elements in a Laminar Boundary Layer," Ph.D. Dissertation, Dept. of Aeronautical and Astronautical Engineering, Univ. of Illinois, Urbana, IL, 1996.